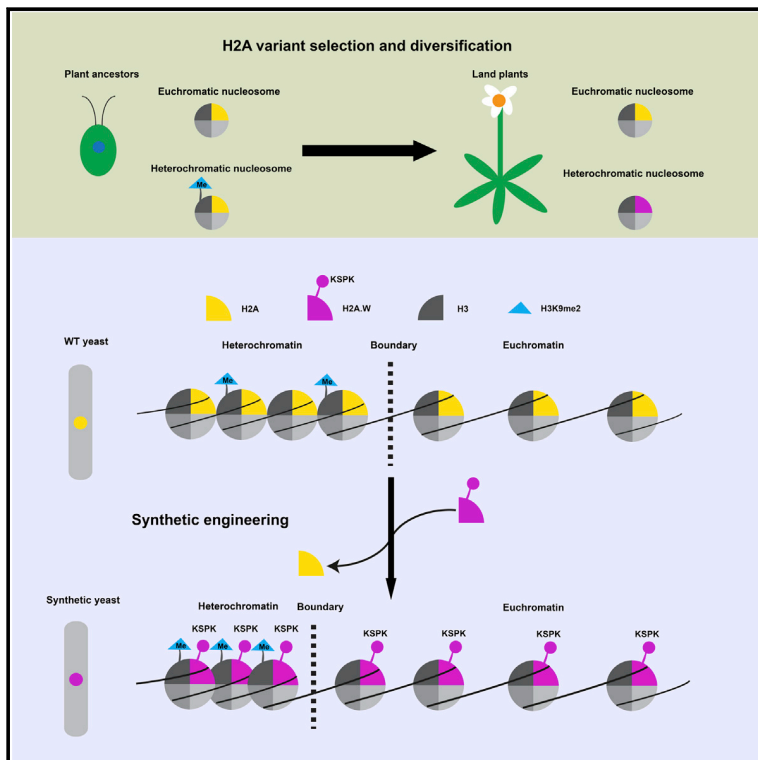# A Synthetic Approach to Reconstruct the Evolutionary and Functional Innovations of the Plant Histone Variant H2A.W

Graphical Abstract

Authors

Bingkun Lei, Matías Capella, Sean A. Montgomery, ..., Abubakar Muhammad, Sigurd Braun, Frédéric Berger

Correspondence

sigurd.braun@bmc.med.lmu.de (S.B.), frederic.berger@gmi.oeaw.ac.at (F.B.)

In Brief

Plants evolved histone H2A.W variants with a KSPK motif, which are segregated to heterochromatin. Lei et al. show that, in yeast, synthetic H2A with a KSPK motif is distributed evenly but impacts only heterochromatin composition, supporting that emergent properties of H2A variants could be selected prior to their segregation to chromatin domains.

Highlights

- Selection of the motif KSPK marks evolution of H2A.W in vascular plants

- Synthetic addition of the KSPK motif to yeast H2A affects only heterochromatin

- Histone variants can be selected prior to their segregation to chromatin domains

CellPress

Report

A Synthetic Approach to Reconstruct the Evolutionary and Functional Innovations of the Plant Histone Variant H2A.W

Bingkun Lei,[1] Matías Capella,[2] Sean A. Montgomery,[1] Michael Borg,[1] Akihisa Osakabe,[1] Malgorzata Goiser,[1] Abubakar Muhammad,[2,3] Sigurd Braun,[2,3,*] and Frédéric Berger[1,4,*]

[1]Gregor Mendel Institute (GMI), Austrian Academy of Sciences, Vienna BioCenter (VBC), Dr. Bohr-Gasse 3, 1030 Vienna, Austria
[2]Biomedical Center, Department of Physiological Chemistry, Ludwig-Maximilians-University of Munich, Großhaderner Straße 9, 82152 Planegg-Martinsried, Germany
[3]International Max Planck Research School for Molecular and Cellular Life Sciences, Am Klopferspitz 18, 82152 Planegg-Martinsried, Germany
[4]Lead Contact
*Correspondence: sigurd.braun@bmc.med.lmu.de (S.B.), frederic.berger@gmi.oeaw.ac.at (F.B.)
https://doi.org/10.1016/j.cub.2020.09.080

SUMMARY

Diversification of histone variants is marked by the acquisition of distinct motifs and functional properties through convergent evolution.[1–4] H2A variants are distinguished by specific C-terminal motifs and tend to be segregated within defined domains of the genome.[5,6] Whether evolution of these motifs pre-dated the evolution of segregation mechanisms or vice versa has remained unclear. A suitable model to address this question is the variant H2A.W, which evolved in plants through acquisition of a KSPK motif[7] and is tightly associated with heterochromatin.[4] We used fission yeast, where chromatin is naturally devoid of H2A.W, to study the impact of engineered chimeras combining yeast H2A with the KSPK motif. Biochemical assays showed that the KSPK motif conferred nucleosomes with specific properties. Despite uniform incorporation of the engineered H2A chimeras in the yeast genome, the KSPK motif specifically affected heterochromatin composition and function. We conclude that the KSPK motif promotes chromatin properties in yeast that are comparable to the properties and function of H2A.W in plant heterochromatin. We propose that the selection of functional motifs confer histone variants with properties that impact primarily a specific chromatin state. The association between a new histone variant and a preferred chromatin state can thus provide a setting for the evolution of mechanisms that segregate the new variant to this state, thereby enhancing the impact of the selected properties of the variant on genome activity.

RESULTS AND DISCUSSION

Histones evolved in the common ancestor of archaea and eukaryotes but assemble into octameric nucleosomes only within the eukaryotic lineage.[8] This defining feature of eukaryotic life drove the evolution of a whole array of new functions, including transcriptional regulation, DNA repair, mitosis, and meiosis.[9] It has been proposed that the diversification of histone variants that accompanies evolution of multicellular eukaryotes enabled more complex modes of regulation of these chromatin activities.[1–3,5,6] Neofunctionalization of histone variants from the H2A family is marked by the acquisition of specific amino acid motifs in their C-terminal tails as well as occupation of very defined chromatin states.[5,6] For example, variants H2A.W in plants and macroH2A in animals are associated with transcriptional repression.[4,10] The mechanisms responsible for segregation of macroH2A and H2A.W to heterochromatin are unknown.[11] Moreover, it remains unclear whether the deposition mechanisms shaping these H2A-marked chromatin states evolved before or after the emergence of H2A variant motifs.

To address this question, we focused on the evolutionary history of H2A.W in flowering plants. We used recently published genomes to generate a new phylogenetic tree of H2A variants in streptophytes, which comprise land plants and algal representatives of their ancestors.[12–15] H2A.Z, replicative H2A, and H2A.X variants are the only representatives of the histone H2A family present in the aquatic ancestors of land plants (Figures 1A and 1B). A distinct fifth type of H2A variant characterized by a longer tail enriched in lysine (K) residues was previously identified as H2A.M in early diverging land plant lineages.[7] In light of recent land plant phylogenies that demonstrate the monophyly of bryophytes,[12,16–18] we refined H2A.M and H2A.W as being restricted to bryophytes and vascular plants, respectively (Figures 1A–1C; Data S1). H2A.W is further distinguished from H2A.M by the presence of a KSPK motif in its C-terminal tail (Figures 1A–1C; Data S1). Although it remains plausible that H2A.M and H2A.W evolved independently, the phylogeny suggests that both variants share a common ancestral sequence with an elongated, K-rich C-terminal tail (Figure 1B). In *Arabidopsis*, H2A.W is present in constitutive heterochromatin marked with di-
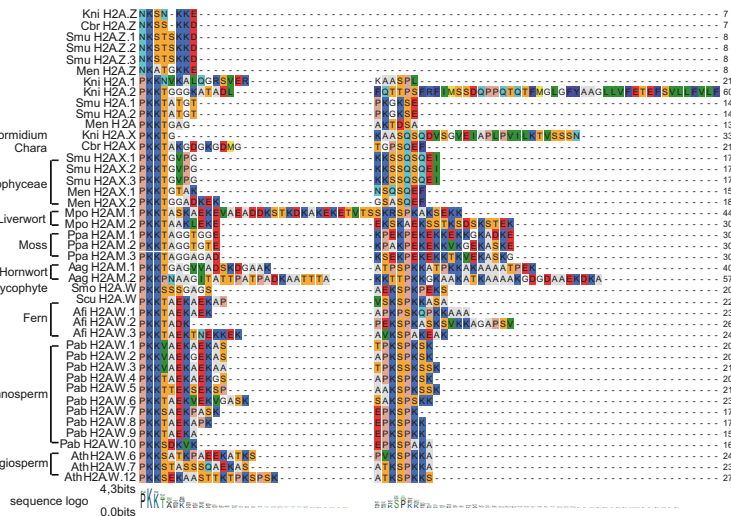
A

H2A.W

H2A.M

H2A.X

H2A.Z

H2A

0.3
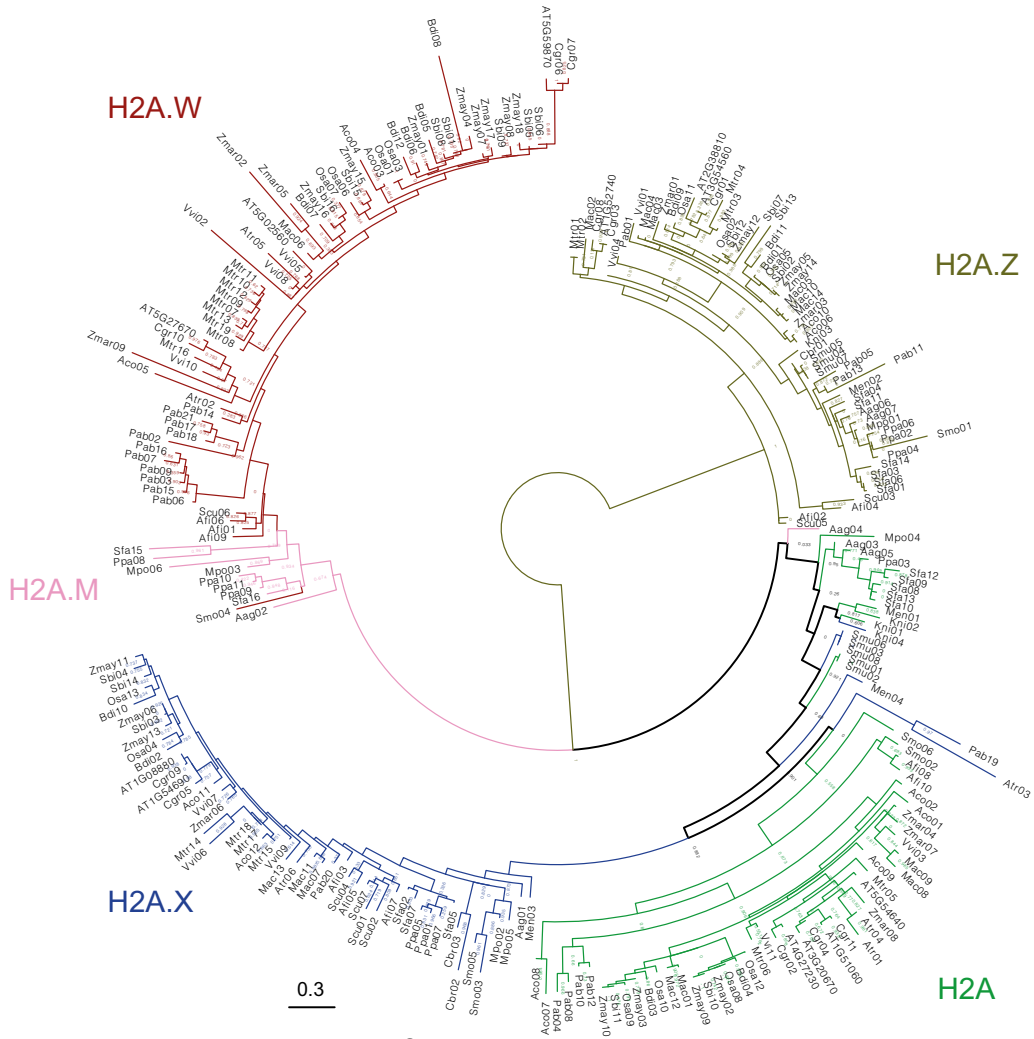
B
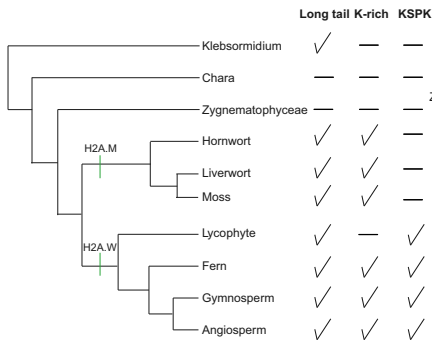
C

(legend on next page)

methylation of H3 lysine 9 (H3K9me2), but the localization of H2A.W in extant representatives of ancestral vascular plants, such as ferns and lycophytes, is unknown. Hence, based on a phylogenetic approach, it is difficult to establish whether the localization of H2A.W to heterochromatin or the KSPK motif evolved first.

The KSPK Motif Affects Chromatin Accessibility by Protecting Linker DNA *In Vitro*

We reasoned that, if the KSPK motif evolved before heterochromatin localization of H2A.W, it likely conferred specific properties to the nucleosome. Thus, to test this idea, we studied the impact of the KSPK motif *in vitro*. Previous studies reported that the physical interaction between linker DNA and the C-terminal tail of H2A variants changes accessibility to micrococcal nuclease (MNase).[19] To investigate whether the KSPK motif directly protects linker DNA, we performed MNase treatment assays with *in vitro* reconstituted *Arabidopsis* nucleosomes containing wild-type H2A.W and H2A.W mutants with either the KSPK motif replaced by four alanine residues (H2A.W4A) or lacking the C-terminal tail (H2A.W.6ΔCT). We used H2A.Z as a control (Figures S1A and S1B). As reported previously,[19] due to the linker DNA protection by the H2A.W-specific extended C-terminal tail, MNase digestion of H2A.W nucleosomes produced primarily four DNA fragments between 130 bp and 165 bp, representing nucleosome core particles in addition to different lengths of linker DNA protected from MNase (Figure S1C). Control H2A.Z nucleosomes, which have a short C-terminal tail, produced hardly any 165-bp fragments but an abundant fraction of 130-bp fragments, which result from over-digestion due to the breathing of DNA ends (Figure S1D). In contrast to H2A.Z, the longer fragments (155 and 165 bp) corresponding to partial digestion by MNase were remarkably abundant when nucleosomes contained H2A.W, but not H2A.WΔCT, suggesting that the C-terminal tail of H2A.W prevents the breathing of DNA ends (Figures S1D–S1F). Compared with H2A.W, H2A.W4A nucleosomes were more susceptible to MNase digestion and showed intermediate properties between H2A.W and H2A.WΔCT (Figures S1D–S1F). These results suggest that the KSPK motif in the C-terminal tail of H2A.W variants augments the capacity to interact with linker DNA, accounting for some part of the impact of the H2A.W C-terminal tail on breathing of DNA ends. Hence, the KSPK motif strengthens contact between H2A.W C-terminal tail and linker DNA and is expected to reduce chromatin accessibility and to limit further the low dynamic exchange of nucleosomes that is observed in heterochromatin.[20]

Using Fission Yeast to Study the Impact of the Synthetic Histone Variant H2A.W C-Terminal Tail on Chromatin

The strong impact of the KSPK motif and the extension of the C-terminal tail on nucleosome properties led us to consider that these features might impact chromatin properties and organization when introduced in a model species that does not encode H2A.W. To study this hypothesis, we engineered the potential evolutionary trajectories of H2A.W in the fission yeast *Schizosaccharomyces pombe*. Fission yeast chromatin contains only H2A.Z encoded by a single gene (*pht1*⁺) and two isoforms of H2A.X (H2A.α and H2A.β), which are encoded by *hta1*⁺ and *hta2*⁺, respectively. Thereafter, we followed commonly used abbreviation spH2A to refer collectively to the isoforms H2A.α and H2A.β. We constructed chimeric histones that combine spH2A with the C-terminal tail of various H2A variants from plants, including *Arabidopsis thaliana* (*At*) and *Marchantia polymorpha* (*Mpo*) (Figure 2A). Homologous recombination was used to replace *hta1*⁺ and *hta2*⁺ with genes encoding chimeras of spH2A with either (1) an extended C-terminal tail consisting of a repetition of the wild-type (WT) C-terminal tail in spH2ACT, (2) a long tail with the KSPK motif in spH2A.W^{At}, (3) a long tail without the KSPK motif in spH2A.W4A^{At}, and (4) the long tails of H2A.M.1 (spH2A.M.1^{Mpo}) or H2A.M.2 (spH2A.M.2^{Mpo}; Figures 2B and S2A). The resulting chimeric histone H2A variants were expressed from the endogenous promoters of *hta1*⁺ and *hta2*⁺ at levels comparable to WT (see STAR Methods and Figure S2B). Expressing these chimeric H2A variants affected neither cell morphology nor growth rate under normal growth conditions (Figures 2C, 2D, and S2C).

Rapid and robust response to environmental stress is critical for cell survival, and growth rates are affected by temperature[21] or the denaturing agent formamide when combined with other deficiencies.[22] We thus performed a serial dilution spot assay to assess the impact of each chimeric H2A on cell survival rates in response to environmental stressors. In contrast to WT, expression of spH2A.W^{At}, which harbors the KSPK motif, caused a severe growth defect in synthetic yeast strains growing at high temperature or on formamide-containing media (Figure 2C; 37°C and 2% formamide). This growth phenotype was not observed with spH2ACT or attenuated when the KSPK motif was swapped to a stretch of four alanine residues (spH2A.W4A^{At}; Figure 2C). Compared to the severe phenotype conferred by spH2A.W^{At}, expression of the other chimeras lacking the KSPK motif (spH2A.M.1^{Mpo} and spH2A.M.2^{Mpo}) caused milder growth defects than spH2A.W^{At} in stressful growth conditions (Figure 2C). We further validated the observed phenotype

---

Figure 1. Land Plants Evolved Twice a Fourth Type of H2A Variant

(A) Maximum-likelihood phylogeny of streptophyte H2A protein sequences. Colors correspond to different H2A variants (pink: H2A.M; dark red: H2A.W; blue: H2A.X; green: replicative H2A; brown: H2A.Z). Approximate likelihood ratio test values based on a Shimodaira-Hasegawa-like procedure are indicated on each node. Scale bar indicates substitutions per site.

(B) Potential H2A.W innovations during streptophyte evolution. Checkmarks indicate the presence of an H2A isoform in each clade with a C-terminal tail greater than 20 amino acid residues but absence of the H2A.X SQE motif (long tail), presence of five or more lysine residues (K-rich), or a KSPK motif (KSPK). Diagram depicts H2A.M and H2A.W histone variants.

(C) Alignment of selected plant H2A C-terminal tails. Lengths of C-terminal tails are indicated to the right of each sequence, and a sequence logo below shows the relative frequency of indicated amino acids per position. Codes for species names are as follows: Kni (*Klebsormidium nitens*); Cbr (*Chara braunii*); Smu (*Spirogloea muscicola*); Men (*Mesotaenium endlicherianum*); Mpo (*Marchantia polymorpha*); Ppa (*Physcomitrella patens*); Aag (*Anthoceros agrestis*); Smo (*Selaginella moellendorffii*); Scu (*Salvinia cucullata*); Afi (*Azolla filiculoides*); Pab (*Picea abies*); and Ath (*Arabidopsis thaliana*).
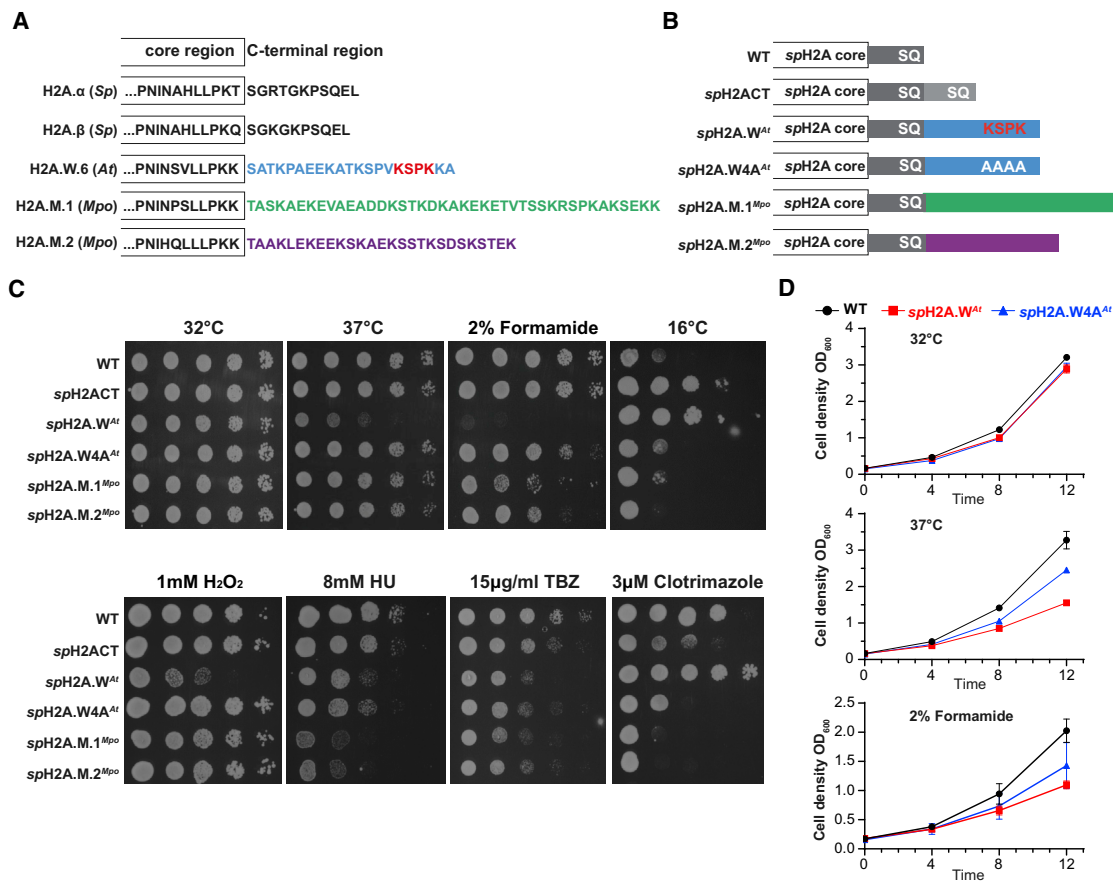
See also Figure S1.

Figure 2. The Impact of the C-Terminal Tail of Plants H2A.M and H2A.W on Fission Yeast Growth

(A) C-terminal sequences of histone H2A.α and H2A.β from *Schizosaccharomyces pombe* (*Sp*), H2A.W C-terminal sequence from *Arabidopsis thaliana* (*At*), and H2A.M C-terminal sequences from Marchantia polymorpha (*Mpo*).

(B) Schematic presentation of histone H2A fusion proteins with different C-terminal sequences shown in (A).

(C) Growth assays of WT and chimeric histone H2A proteins. 5-fold serial dilutions of WT and the indicated engineered yeast mutants were grown at the indicated temperature or in presence of formamide, hydrogen peroxide (H_2O_2), thiabendazole (TBZ), hydroxyurea (HU), or clotrimazole.

(D) Growth curves of the indicated yeast strains in liquid media at 32°C and 37°C or in media supplemented with 2% v/v formamide. Normalized scores by initial cell numbers and averaged from two biological replicates are plotted.

See also Figure S2.

for WT, *sp*H2A.W^{At}, and *sp*H2A.W4A^{At} cells by measuring growth curves in liquid media under normal growth conditions at 32°C, 37°C, or with formamide (Figure 2D). We also extended the range of stresses tested and observed that *sp*H2A.W^{At} was more sensitive to the ribonucleotide reductase inhibitor hydroxyurea (HU), microtubule destabilizing drug thiabendazole (TBZ), and hydrogen peroxide (H_2O_2), the latter one being KSPK specific (Figure 2C). By contrast, *sp*H2A.W^{At} was more tolerant to cold (16°C) and to the antifungal drug clotrimazole.

Previous studies have shown that upregulation of fast-evolving genes present in subtelomeric heterochromatin of yeast modulates survival in stressful conditions.[23–25] This led us to investigate the impact of *sp*H2A.W^{At} on gene expression. We performed RNA sequencing (RNA-seq) analysis in WT and *sp*H2A.W^{At} strains in the presence or absence of formamide and observed changes of expression levels for less than a hundred genes (Figures S3A and S3B). The mild impact of *sp*H2A.W^{At} on transcription was also in agreement with the

very limited impact of *sp*H2A.W^{At} on chromatin accessibility assessed by assay for transposase-accessible chromatin using sequencing (ATAC-seq) (Figure S3C). Downregulated genes were mostly involved in RNA metabolism, in agreement with a previous study on the impact of formamide in mutant backgrounds (Data S2).[22] In conclusion, the chimera mimicking H2A.W affected yeast growth under various stress conditions, suggesting that the long C-terminal tail or the KSPK motif confers novel and specific functions to the chimeric H2A variant in fission yeast.

H2A.W Impacts the Boundary between Euchromatin and Heterochromatin

Upregulated genes, which made up the large fraction of misregulated transcripts in the synthetic strain *sp*H2A.W^{At}, were significantly more likely to be located within subtelomeric heterochromatin of chromosomes I and II, near to the boundary between heterochromatin and euchromatin, or clustered on
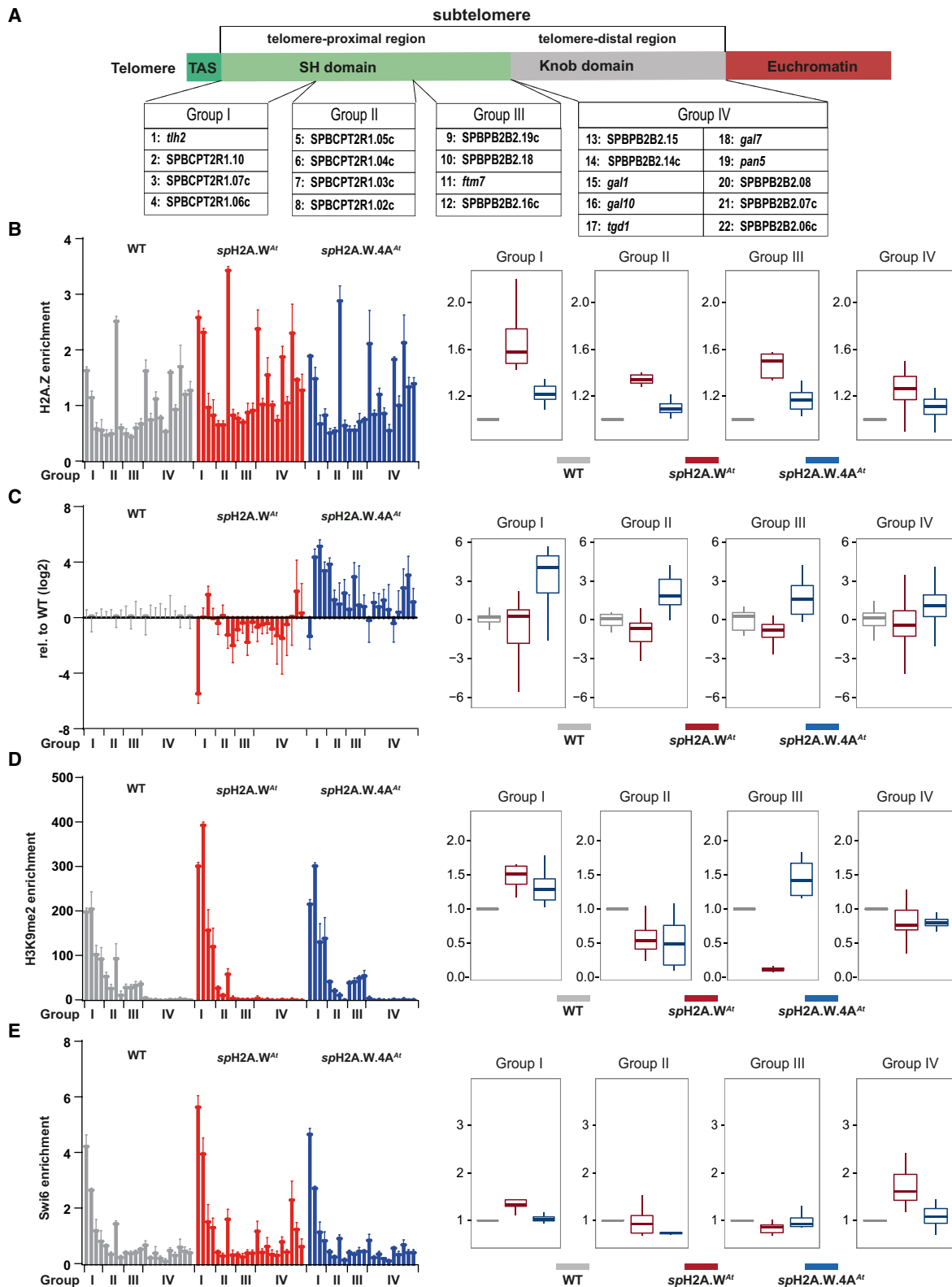
Figure 3. The Impact of H2A.W C-Terminal Tail Impacts on Gene Expression and Chromatin Composition in Subtelomeres

(A) Scheme of subtelomere organization in *S. pombe*. Adjacent to the telomere-associated sequences (TASs) (dark green) is the subtelomeric homologous region (SH) (:50 kb; light green), which is marked by H3K9me2 and shares high similar sequence identity (>98%) between chromosomal arms I and II. The telomere-distal

(legend continued on next page)

chromosomes II and III (Figure S3A; Data S2; odds ratio = 49.497; Fisher's exact p < 2.2e−16). This observation suggested that *sp*H2A.W^{At} perturbed the local chromatin environment of subtelomeric heterochromatin. To test this idea, we explored the impact of *sp*H2A.W^{At} on the profiles of H2A.Z, H3K9me2, and its reader Swi6 (the homolog of mammalian HP1).[26,27] First, to rule out that the KSPK motif causes localized variation of histone incorporation in *sp*H2A.W^{At}, we confirmed that *sp*H2A.W^{At} was evenly incorporated along chromosomes in the synthetic strain, like *sp*H2A in WT (Figure S3D). Then, to quantify precisely the impact of *sp*H2A.W^{At} and *sp*H2A.W4A^{At} on subtelomeric heterochromatin, we used ChIP followed by qPCR to explore the two subtelomeric domains adjacent to the region next to the telomeric repeats of TEL2R, which is best annotated among all chromosomal arms in *S. pombe* (Figure 3A). These subtelomeric domains are the telomere-proximal region enriched in H3K9me2 (also known as subtelomeric homologous region [SH]) and the distal region, which is relatively depleted of H3K9me2, borders euchromatin, and forms compact subnuclear structures defined as ''knob chromatin'' (Figure 3A).[28] ChIP qPCR results are presented for 22 individual loci along subtelomere 2R and summarized in distinct groups (shown as boxplots) based on their location (Figure 3A). We used ChIP-qPCR to study the impact of *sp*H2A.W^{At} and *sp*H2A.W4A^{At} on the profiles of H2A.Z, H3K9me2, and Swi6 (Figures 3B, 3D, and 3E). In addition, we explored gene expression changes relative to WT by RT-qPCR for these subtelomeric loci (Figure 3C).

Overall, the four parameters studied were affected primarily in loci from the SH region (groups I–III; Figure 3) with the exception of H2A.Z enrichment, which increased in a uniform manner over subtelomeres, and this increase was much stronger in *sp*H2A.W^{At} than in *sp*H2A.W4A^{At} (Figures 3B and S3E). Although H2A.Z enrichment in euchromatin correlates positively with transcription,[29] we rather observed an anticorrelation between the marked invasion of subtelomeric heterochromatin by H2A.Z in *sp*H2A.W^{At} and further repression of transcription at the majority of loci in subtelomeric regions (Figures 3B and 3C). Several loci in groups I and III were more transcriptionally repressed (Figure 3C) and gained enrichment in H3K9me2 and its reader Swi6, although with a more reduced amplitude of the latter (Figures 3D and 3E). Hence, we propose that the conjugated impacts of the

KSPK motif and a longer C-terminal tail enriched in lysine residues of *sp*H2A.W^{At} prevent the dynamic exchange that clears H2A.Z from the SH domain with consequences on the accumulation of H3K9me2 and gene expression.

The KSPK Motif Directly Impacts Heterochromatin Properties in Fission Yeast

Because the KSPK introduction in *sp*H2A into subtelomeric chromatin had a strong impact on regions most enriched in H3K9me2 represented by group I loci, we extended our analyses to similar regions by studying the outer repeats (*otr*) of pericentromeric heterochromatin (Figure 4A). We observed a significant enrichment of H3K9me2 at the pericentromeric *dg* and *dh* repeats in *sp*H2A.W^{At}, but not *sp*H2A.W4A^{At}, compared to WT (Figures 4B and S4A). In contrast, the centromeric core region (*cnt1$^+$*) that is devoid of H3K9me2/3 was not affected in *sp*H2A.W^{At} or in *sp*H2A.W4A^{At} (Figure 4B). We did not observe significant differences in transcript levels of *dg* and *dh* at pericentromeric heterochromatin, which are tightly repressed in WT cells. However, we found that transcription from the centromeric *cnt* domain was more repressed in *sp*H2A.W^{At} in comparison to WT and *sp*H2A.W4A^{At} (Figure 4C). Similarly, the *ura4$^+$* gene, when inserted into the less tightly repressed pericentromeric *imr1L* locus, displayed stronger silencing in the *sp*H2A.W^{At} strain than in WT cells (Figure 4D). In addition, we examined islands of facultative heterochromatin that accumulate H3K9me2 in response to stress[30] and detected three islands enriched in H3K9me2 in *sp*H2A.W^{At}, but not in WT and *sp*H2A.W4A^{At} (Figures 4E and 4F). These heterochromatin islands are distinct from that forming in response to cold in the WT,[31] but considering that *sp*H2A.W^{At} confers resistance to cold treatment, it might change the adaptive genome control shown previously.[31] It would be interesting to investigate the formation of heterochromatin islands and adaptive response of the genome in cold and other stress conditions conferred by *sp*H2A.W^{At}.

Hence, we conclude that the KSPK motif of H2A.W is sufficient to promote enrichment in H3K9me2 and, as a consequence, more robust gene silencing. In agreement, we found that the strong hyper-silencing phenotype at telomere-proximal chromatin *sp*H2A.W^{At} is completely alleviated in the absence of the Snf2-like histone deacetylase (HDAC)-containing repressor complex SHREC or the methyltransferase Clr4,

---

region (gray) displays only little sequence similarity and is largely devoid of histone modifications. This region also contains condensed chromatin structures known as knob chromatin. The red box depicts euchromatin. Genes from the subtelomeres have been divided into four groups, depending on their location and distinct H3K9me2 pattern in WT, *sp*H2A.W^{At}, and *sp*H2A.W4A^{At} yeast strains.

(B) ChIP-qPCR analysis of enrichment in H2A.Z at gene loci from groups I–IV at the subtelomere 2R region in WT, *sp*H2A.W^{At}, and *sp*H2A.W4A^{At} yeast strains. ChIP signals are shown as fold enrichment relative to *act1$^+$*, after normalization to input. Values were corrected for histone abundance by normalizing to the mean of loci for H3 ChIP fold enrichment. Bars show mean values of two independent biological experiments (error bars: deviation from the mean). Boxplots show grouped summary presentation of individual genomic loci (groups I–IV) based on their distinct H3K9me2 pattern from all biological experiments. For groups I–III, 4 genes each were selected; for group IV, 10 genes were selected (for individual genes, see A).

(C) Transcript levels of gene loci highlighted in groups I–IV at subtelomere 2R region in WT, *sp*H2A.W^{At}, and *sp*H2A.W4A^{At} yeast strains. Transcript levels have been normalized to *act1$^+$*, and the bar graph shows the mean of four independent biological experiments relative to the mean of WT (error bars: SD). Boxplots show grouped summary presentation as in (B).

(D and E) ChIP-qPCR analysis of enrichment in H3K9me2 and Swi6 at gene loci from groups I–IV at the subtelomere 2R region in WT, *sp*H2A.W^{At}, and *sp*H2A.W4A^{At} yeast strains. ChIP signals are shown as fold enrichment relative to *act1$^+$*, after normalization to input. Values were corrected for histone abundance by normalizing to the mean of loci for H3 ChIP fold enrichment. Bars show mean values of two independent biological experiments (error bars: deviation from the mean). Boxplots show grouped summary presentation as in (B).
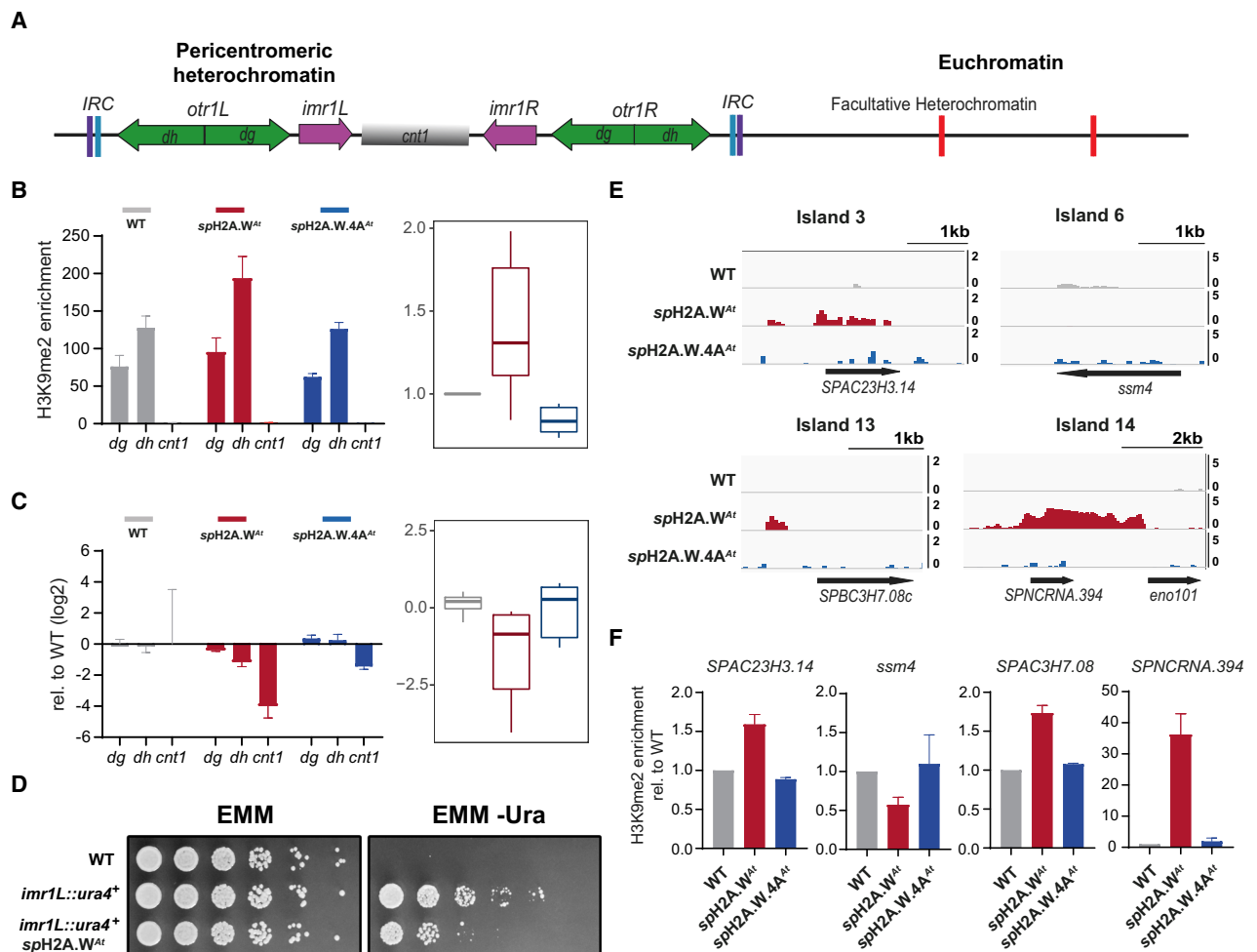
See also Figure S3 and Data S2.

Figure 4. The KSPK Motif of Histone H2A.W Directly Impacts Heterochromatin Properties

(A) Scheme of pericentromeric heterochromatin and facultative heterochromatin. *cnt1*, central core of centromere 1; *dg* and *dh*, repeat elements in *otr1*; *imr1*, innermost repeat 1; *IRC*, centromeric inverted repeat element; *otr1*, outer repeat 1.

(B) Levels of H3K9me2 enrichment at pericentromeric heterochromatin loci. ChIP signals are shown as fold enrichment relative to *act1*+, after normalization to input. Values were corrected for histone abundance by normalizing to the mean of loci for H3 ChIP fold enrichment. Bars show mean values of two independent biological experiments (error bars: deviation from the mean). Boxplot shows grouped summary presentation of individual genomic loci relative to WT.

(C) Transcript levels at pericentromeric heterochromatin in WT, *sp*H2A.W^{At}, and *sp*H2A.W4A^{At} strains. Data have been normalized to *act1*+, and the bar graph shows the mean of four independent biological experiments relative to the mean of WT (error bars: SD). Boxplots show the $\log_2$ fold change for all pericentromeric heterochromatin loci analyzed.

(D) Silencing reporter gene assay at pericentromeric *imr1L* locus. Cultures of indicated yeast strains were spotted in 5-fold serial dilutions onto Edinburgh minimal medium (EMM) and EMM-Ura and grown at 32°C for 3 days.

(E) Genome browser plot illustrating normalized H3K9me2 ChIP-seq reads mapping to different heterochromatin islands in WT, *sp*H2A.W^{At}, or *sp*H2A.W4A^{At}.

(F) Bar plot showing H3K9me2 enrichment of selected gene loci at heterochromatin islands in WT, *sp*H2A.W^{At}, and *sp*H2A.W4A^{At} strains. Values were corrected for histone abundance by normalizing to the mean of loci for H3 ChIP fold enrichment. Bars show mean values of two independent biological experiments (error bars: deviation from the mean).

See also Figure S4.

which is the sole enzyme that deposits H3K9 methylation in *S. pombe* (Figure S4B). H3K9me2/3 opposes nucleosome dynamics, and our results suggest that this histone modification acts in synergy with the nucleosome-stabilizing properties conferred by H2A.W in heterochromatin to oppose the action of transcription and H2A.Z incorporation that mark euchromatin. We propose that the KSPK motif enhances nucleosome stability and reduces further the dynamic exchange of nucleosomes in heterochromatin, thus promoting accumulation

of heterochromatic marks leading to the transcriptional silencing of genes embedded in heterochromatin in various contexts.

Conclusions

Expression of chimeric H2A variants with a long C-terminal tail and KSPK motif in yeast heterochromatin has an impact comparable to the repressive role ascribed to H2A.W in *Arabidopsis* heterochromatin.[4] Remarkably, in yeast, the KSPK motif does

not constrain the location of the variant spH2A.W^{At} to heterochromatin and yet primarily affects only heterochromatin properties. In conclusion, synthetic reconstruction of H2A.W variant evolution in yeast supports the potential for emergence of the motif KSPK prior to mechanisms responsible for segregation of H2A.W to heterochromatin. The KSPK motif has been also selected in macroH2A variants, which are also present in heterochromatin in animals,[2,6] as well as in sperm-specific H2B variants in sea urchin.[32] All these variants are associated with chromatin condensation, supporting further that convergent evolution operates in selection of histone variants.[2,11] More broadly, this work provides insight into the mode of histone variant evolution and their deposition mechanisms. The association of a new histone variant with a specific chromatin environment creates the prerequisite for the evolution and selection of particular deposition mechanisms, thereby enhancing the impact of the properties associated with the variant on genome activity (Figure S4C). Such an evolutionary scheme will participate in understanding how more-complex organization of chromatin arose during evolution of eukaryotes.

STAR★METHODS

Detailed methods are provided in the online version of this paper and include the following:

- KEY RESOURCES TABLE
- RESOURCE AVAILABILITY
  - Lead Contact
  - Materials Availability
  - Data and Code Availability
- EXPERIMENTAL MODEL AND SUBJECT DETAILS
  - *S. pombe* strains and culture conditions
- METHOD DETAILS
  - MNase treatment assay
  - Phylogenetic analysis
  - Multiple sequence analysis
  - Construction of the yeast strains
  - Yeast growth sensitivity assay
  - Histone extraction assay
  - Live cell microscopy and imaging
  - Transcriptome library preparation, sequencing and analysis
  - Chromatin immunoprecipitation (ChIP)
  - ChIP library preparation, sequencing, and analysis
  - ATAC-seq

SUPPLEMENTAL INFORMATION

Supplemental Information can be found online at https://doi.org/10.1016/j.cub.2020.09.080.

AUTHOR CONTRIBUTIONS

M.C. and A.M. performed RT-qPCR experiments. S.A.M. obtained the phylogenetic analysis. A.O. assisted experiments in Figure S1. M.B. analyzed the ATAC-seq results. M.G. analyzed the RNA-seq and ChIP-seq results. B.L. performed all other experiments. F.B. and S.B. conceived the project. F.B., B.L., and S.B. wrote the manuscript, and all authors participated in revisions.

DECLARATION OF INTERESTS

The authors declare no competing interests.

REFERENCES

1. Talbert, P.B., and Henikoff, S. (2017). Histone variants on the move: substrates for chromatin dynamics. Nat. Rev. Mol. Cell Biol. *18*, 115–126.

2. Talbert, P.B., Ahmad, K., Almouzni, G., Ausió, J., Berger, F., Bhalla, P.L., Bonner, W.M., Cande, W.Z., Chadwick, B.P., Chan, S.W.L., et al. (2012). A unified phylogeny-based nomenclature for histone variants. Epigenetics Chromatin *5*, 7.

3. Malik, H.S., and Henikoff, S. (2003). Phylogenomics of the nucleosome. Nat. Struct. Biol. *10*, 882–891.

4. Yelagandula, R., Stroud, H., Holec, S., Zhou, K., Feng, S., Zhong, X., Muthurajan, U.M., Nie, X., Kawashima, T., Groth, M., et al. (2014). The histone variant H2A.W defines heterochromatin and promotes chromatin condensation in Arabidopsis. Cell *158*, 98–109.

5. Lei, B., and Berger, F. (2020). H2A variants in Arabidopsis: versatile regulators of genome activity. Plant Commun. *1*, 100015.

6. Bönisch, C., and Hake, S.B. (2012). Histone H2A variants in nucleosomes and chromatin: more or less stable? Nucleic Acids Res. *40*, 10719–10741.

7. Kawashima, T., Lorković, Z.J., Nishihama, R., Ishizaki, K., Axelsson, E., Yelagandula, R., Kohchi, T., and Berger, F. (2015). Diversification of histone H2A variants during plant evolution. Trends Plant Sci. *20*, 419–425.

8. Henneman, B., van Emmerik, C., van Ingen, H., and Dame, R.T. (2018). Structure and function of archaeal histones. PLoS Genet. *14*, e1007582.

9. Henikoff, S., and Smith, M.M. (2015). Histone variants and epigenetics. Cold Spring Harb. Perspect. Biol. *7*, a019364.

10. Kozlowski, M., Corujo, D., Hothorn, M., Guberovic, I., Mandemaker, I.K., Blessing, C., Sporn, J., Gutierrez-Triana, A., Smith, R., Portmann, T., et al. (2018). MacroH2A histone variants limit chromatin plasticity through two distinct mechanisms. EMBO Rep. *19*, e44445.

11. Drinnenberg, I.A., Berger, F., Elsässer, S.J., Andersen, P.R., Ausió, J., Bickmore, W.A., Blackwell, A.R., Erwin, D.H., Gahan, J.M., Gaut, B.S., et al. (2019). EvoChromo: towards a synthesis of chromatin biology and evolution. Development *146*, Dev178962.

12. Li, F.-W., Nishiyama, T., Waller, M., Frangedakis, E., Keller, J., Li, Z., Fernandez-Pozo, N., Barker, M.S., Bennett, T., Blázquez, M.A., et al. (2020). Anthoceros genomes illuminate the origin of land plants and the unique biology of hornworts. Nat. Plants *6*, 259–272.

13. Cheng, S., Xian, W., Fu, Y., Marin, B., Keller, J., Wu, T., Sun, W., Li, X., Xu, Y., Zhang, Y., et al. (2019). Genomes of subaerial zygnematophyceae provide insights into land plant evolution. Cell *179*, 1057–1067.e14.

14. Nishiyama, T., Sakayama, H., de Vries, J., Buschmann, H., Saint-Marcoux, D., Ullrich, K.K., Haas, F.B., Vanderstraeten, L., Becker, D., Lang, D., et al. (2018). The Chara Genome: secondary complexity and implications for plant terrestrialization. Cell *174*, 448–464.e24.

15. Lang, D., Ullrich, K.K., Murat, F., Fuchs, J., Jenkins, J., Haas, F.B., Piednoel, M., Gundlach, H., Van Bel, M., Meyberg, R., et al. (2018). The Physcomitrella patens chromosome-scale assembly reveals moss genome structure and evolution. Plant J. *93*, 515–533.

16. de Sousa, F., Foster, P.G., Donoghue, P.C.J., Schneider, H., and Cox, C.J. (2019). Nuclear protein phylogenies support the monophyly of the three bryophyte groups (Bryophyta Schimp.). New Phytol. *222*, 565–575.

17. Puttick, M.N., Morris, J.L., Williams, T.A., Cox, C.J., Edwards, D., Kenrick, P., Pressel, S., Wellman, C.H., Schneider, H., Pisani, D., and Donoghue, P.C.J. (2018). The interrelationships of land plants and the nature of the ancestral embryophyte. Curr. Biol. *28*, 733–745.e2.

18. Liu, Y., Johnson, M.G., Cox, C.J., Medina, R., Devos, N., Vanderpoorten, A., Hedenäs, L., Bell, N.E., Shevock, J.R., Aguero, B., et al. (2019). Resolution of the ordinal phylogeny of mosses using targeted exons from organellar and nuclear genomes. Nat. Commun. *10*, 1485.

19. Osakabe, A., Lorkovic, Z.J., Kobayashi, W., Tachiwana, H., Yelagandula, R., Kurumizaka, H., and Berger, F. (2018). Histone H2A variants confer specific properties to nucleosomes and impact on chromatin accessibility. Nucleic Acids Res. *46*, 7675–7685.

20. Aygün, O., Mehta, S., and Grewal, S.I.S. (2013). HDAC-mediated suppression of histone turnover promotes epigenetic stability of heterochromatin. Nat. Struct. Mol. Biol. *20*, 547–554.

21. Chen, D., Toone, W.M., Mata, J., Lyne, R., Burns, G., Kivinen, K., Brazma, A., Jones, N., and Bähler, J. (2003). Global transcriptional responses of fission yeast to environmental stress. Mol. Biol. Cell *14*, 214–229.

22. Hoyos-Manchado, R., Reyes-Martín, F., Rallis, C., Gamero-Estévez, E., Rodríguez-Gómez, P., Quintero-Blanco, J., Bähler, J., Jiménez, J., and Tallada, V.A. (2017). RNA metabolism is the primary target of formamide in vivo. Sci. Rep. *7*, 15895.

23. Harvey, Z.H., Chakravarty, A.K., Futia, R.A., and Jarosz, D.F. (2020). A prion epigenetic switch establishes an active chromatin state. Cell *180*, 928–940.e14.

24. Brown, C.A., Murray, A.W., and Verstrepen, K.J. (2010). Rapid expansion and functional divergence of subtelomeric gene families in yeasts. Curr. Biol. *20*, 895–903.

25. Ai, W., Bertram, P.G., Tsang, C.K., Chan, T.-F., and Zheng, X.F.S. (2002). Regulation of subtelomeric silencing during stress response. Mol. Cell *10*, 1295–1305.

26. Grewal, S.I.S., and Moazed, D. (2003). Heterochromatin and epigenetic control of gene expression. Science *301*, 798–802.

27. Jacobs, S.A., and Khorasanizadeh, S. (2002). Structure of HP1 chromodomain bound to a lysine 9-methylated histone H3 tail. Science *295*, 2080–2083.

28. Tashiro, S., Nishihara, Y., Kugou, K., Ohta, K., and Kanoh, J. (2017). Subtelomeres constitute a safeguard for gene expression and chromosome homeostasis. Nucleic Acids Res. *45*, 10333–10349.

29. Zofall, M., Fischer, T., Zhang, K., Zhou, M., Cui, B., Veenstra, T.D., and Grewal, S.I.S. (2009). Histone H2A.Z cooperates with RNAi and heterochromatin factors to suppress antisense RNAs. Nature *461*, 419–422.

30. Zofall, M., Yamanaka, S., Reyes-Turcu, F.E., Zhang, K., Rubin, C., and Grewal, S.I. (2012). RNA elimination machinery targeting meiotic mRNAs promotes facultative heterochromatin formation. Science *335*, 96–100.

31. Gallagher, P.S., Larkin, M., Thillainadesan, G., Dhakshnamoorthy, J., Balachandran, V., Xiao, H., Wellman, C., Chatterjee, R., Wheeler, D., and Grewal, S.I.S. (2018). Iron homeostasis regulates facultative heterochromatin assembly in adaptive genome control. Nat. Struct. Mol. Biol. *25*, 372–383.

32. Ausio, J., and Van Holde, K.E. (1988). The histones of the sperm of Spisula solidissima include a novel, cysteine-containing H-1 histone. Cell Differ. *23*, 175–189.

33. Martin, M. (2011). Cutadapt removes adapter sequences from high-throughput sequencing reads. EMBnet.journal *17*, https://doi.org/10.14806/ej.17.1.200.

34. Langmead, B., Trapnell, C., Pop, M., and Salzberg, S.L. (2009). Ultrafast and memory-efficient alignment of short DNA sequences to the human genome. Genome Biology *10*, R25.

35. Ramírez, F., Ryan, D.P., Grüning, B., Bhardwaj, V., Kilpert, F., Richter, A.S., et al. (2016). deepTools2: a next generation web server for deep-sequencing data analysis. Nucleic. Acids Res. *44*, W160–W165.

36. Li, H., Handsaker, B., Wysoker, A., Fennell, T., Ruan, J., Homer, N., Marth, G., Abecasis, G., and Durbin, R.; 1000 Genome Project Data Processing Subgroup (2009). The Sequence Alignment/Map format and SAMtools. Bioinformatics *25*, 2078–2079.

37. Quinlan, A.R., and Hall, I.M. (2010). BEDTools: a flexible suite of utilities for comparing genomic features. Bioinformatics *26*, 841–842.

38. Robinson, J.T., Thorvaldsdóttir, H., Winckler, W., Guttman, M., Lander, E.S., Getz, G., et al. (2011). Integrative genomics viewer. Nature Biotechnology *29*, 24–26.

39. Dobin, A., Davis, C.A., Schlesinger, F., Drenkow, J., Zaleski, C., Jha, S., et al. (2012). STAR: ultrafast universal RNA-seq aligner. Bioinformatics *29*, 15–21.

40. Anders, S., Pyl, P.T., and Huber, W. (2014). HTSeq—a Python framework to work with high-throughput sequencing data. Bioinformatics *31*, 166–169.

41. Schneider, C.A., Rasband, W.S., and Eliceiri, K.W. (2012). NIH Image to ImageJ: 25 years of image analysis. Nature Methods *9*, 671–675.

42. Zhang, Y., Liu, T., Meyer, C.A., Eeckhoute, J., Johnson, D.S., Bernstein, B.E., Nusbaum, C., Myers, R.M., Brown, M., Li, W., and Liu, X.S. (2008). Model-based analysis of ChIP-seq (MACS). Genome Biol. *9*, R137.

43. Ekwall, K., and Thon, G. (2017). Spore analysis and tetrad dissection of Schizosaccharomyces pombe. Cold Spring Harb. Protoc. *2017*, pdb.prot091710.

44. Arimura, Y., Tachiwana, H., Oda, T., Sato, M., and Kurumizaka, H. (2012). Structural analysis of the hexasome, lacking one histone H2A/H2B dimer from the conventional nucleosome. Biochemistry *51*, 3302–3309.

45. Molaro, A., and Drinnenberg, I.A. (2018). Studying the evolution of histone variants using phylogeny. In Histone Variants: Methods and Protocols, G.A. Orsi and G. Almouzni, eds. (Springer), pp. 273–291.

46. Altschul, S.F., Madden, T.L., Schäffer, A.A., Zhang, J., Zhang, Z., Miller, W., and Lipman, D.J. (1997). Gapped BLAST and PSI-BLAST: a new generation of protein database search programs. Nucleic Acids Res. *25*, 3389–3402.

47. Montgomery, S.A., Tanizawa, Y., Galik, B., Wang, N., Ito, T., Mochizuki, T., Akimcheva, S., Bowman, J.L., Cognat, V., Maréchal-Drouard, L., et al. (2020). Chromatin organization in early land plants reveals an ancestral association between H3K27me3, transposons, and constitutive heterochromatin. Curr. Biol. *30*, 573–588.e7.

48. Bowman, J.L., Kohchi, T., Yamato, K.T., Jenkins, J., Shu, S., Ishizaki, K., Yamaoka, S., Nishihama, R., Nakamura, Y., Berger, F., et al. (2017). Insights into land plant evolution garnered from the Marchantia polymorpha genome. Cell *171*, 287–304.e15.

49. Hori, K., Maruyama, F., Fujisawa, T., Togashi, T., Yamamoto, N., Seo, M., Sato, S., Yamada, T., Mori, H., Tajima, N., et al. (2014). Klebsormidium flaccidum genome reveals primary factors for plant terrestrial adaptation. Nat. Commun. *5*, 3978.

50. Nystedt, B., Street, N.R., Wetterbom, A., Zuccolo, A., Lin, Y.-C., Scofield, D.G., Vezzi, F., Delhomme, N., Giacomello, S., Alexeyenko, A., et al. (2013). The Norway spruce genome sequence and conifer genome evolution. Nature *497*, 579–584.

51. Banks, J.A., Nishiyama, T., Hasebe, M., Bowman, J.L., Gribskov, M., dePamphilis, C., Albert, V.A., Aono, N., Aoyama, T., Ambrose, B.A., et al. (2011). The Selaginella genome identifies genetic changes associated with the evolution of vascular plants. Science *332*, 960–963.

52. Katoh, K., and Standley, D.M. (2013). MAFFT multiple sequence alignment software version 7: improvements in performance and usability. Mol. Biol. Evol. *30*, 772–780.

53. Darriba, D., Taboada, G.L., Doallo, R., and Posada, D. (2011). ProtTest 3: fast selection of best-fit models of protein evolution. Bioinformatics *27*, 1164–1165.

54. Guindon, S., Dufayard, J.-F., Lefort, V., Anisimova, M., Hordijk, W., and Gascuel, O. (2010). New algorithms and methods to estimate maximum-likelihood phylogenies: assessing the performance of PhyML 3.0. Syst. Biol. *59*, 307–321.

55. Hordijk, W., and Gascuel, O. (2005). Improving the efficiency of SPR moves in phylogenetic tree search methods based on maximum likelihood. Bioinformatics *21*, 4338–4347.

56. Gregan, J., Rabitsch, P.K., Rumpf, C., Novatchkova, M., Schleiffer, A., and Nasmyth, K. (2006). High-throughput knockout screen in fission yeast. Nat. Protoc. *1*, 2457–2464.

57. Pidoux, A., Mellone, B., and Allshire, R. (2004). Analysis of chromatin in fission yeast. Methods *33*, 252–259.

58. Braun, S., Garcia, J.F., Rowley, M., Rougemaille, M., Shankar, S., and Madhani, H.D. (2011). The Cul4-Ddb1(Cdt)^2 ubiquitin ligase inhibits invasion of a boundary-associated antisilencing factor into heterochromatin. Cell *144*, 41–54.

59. Buenrostro, J.D., Wu, B., Chang, H.Y., and Greenleaf, W.J. (2015). ATAC-seq: a method for assaying chromatin accessibility genome-wide. Curr. Protoc. Mol. Biol. *109*, 21.29.1–21.29.9.

60. Picelli, S., Faridani, O.R., Björklund, Å.K., Winberg, G., Sagasser, S., and Sandberg, R. (2014). Full-length RNA-seq from single cells using Smart-seq2. Nat. Protoc. *9*, 171–181.

61. Langmead, B., and Salzberg, S.L. (2012). Fast gapped-read alignment with Bowtie 2. Nat. Methods *9*, 357–359.

62. Ramírez, F., Dündar, F., Diehl, S., Grüning, B.A., and Manke, T. (2014). deepTools: a flexible platform for exploring deep-sequencing data. Nucleic Acids Res. *42*, W187–W191.

63. Gu, Z., Eils, R., Schlesner, M., and Ishaque, N. (2018). EnrichedHeatmap: an R/Bioconductor package for comprehensive visualization of genomic signal associations. BMC Genomics *19*, 234.

STAR★METHODS

KEY RESOURCES TABLE

REAGENT or RESOURCE	SOURCE	IDENTIFIER
Antibodies		
Rabbit polyclonal anti-H2A	Active Motif	Cat# 39235, RRID: AB_2687477
Rabbit polyclonal anti-H3	Abcam	Cat# ab1791, RRID: AB_302613
Mouse monoclonal anti-H3K9me2	Abcam	Cat# ab1220, RRID: AB_449854
Rabbit polyclonal anti-Swi6	Abcam	Cat# ab188276
Rabbit polyclonal anti-H2A.Z	Active Motif	Cat# 39640, RRID: AB_2793287
Bacterial and Virus Strains		
E. coli strain DH5α	Lab stock	N/A
E. coli strain BL21 (DE3) codonplusRIL	Lab stock	N/A
E. coli strain JM109 (DE3) codonplusRIL	Lab stock	N/A
Chemicals, Peptides, and Recombinant Proteins		
Formamide	AppliChem	Cat# A3606
Nourseothricin	Jena Bioscience	Cat# AB-102L
Hygromycin B solution	AppliChem	Cat# A2175
cOmplete Protease Inhibitor Cocktail	Roche	Cat# 05056489001
RNase A	ThermoFisher Scientific	Cat# EN0531
Proteinase K	ThermoFisher Scientific	Cat# EO0491
Zymolyase	ZYMO RESEARCH	Cat# E1005
Micrococcal Nuclease	New England Biolabs	Cat# M0247S
SYBR Green I Nucleic Acid Gel Stain	Invitrogen	Cat# S7563
NEBNext High-Fidelity 2x PCR Master Mix	New England Biolabs	Cat# M0541S
Recombinant *Arabidopsis* core histones	Osakabe et al.[19]	N/A
Recombinant *Arabidopsis* H2A.W4A	This paper	N/A
Critical Commercial Assays		
RNeasy Plus Mini Kit	QIAGEN	Cat# 74136
DNA Clean & Concentrator™-5	ZYMO RESEARCH	Cat# D4004
NEBNext® Ultra II DNA Library Prep Kit	New England Biolabs	Cat# E7645L
Deposited Data		
ChIP-seq, RNA-seq and ATAC-seq data	This paper	https://www.ncbi.nlm.nih.gov/geo/query/acc.cgi?acc=GSE152086
Experimental Models: Organisms/Strains		
All *S. pombe* strains used in this study	Lab Stocks and this paper	See Table S1

(Continued on next page)

Continued

REAGENT or RESOURCE	SOURCE	IDENTIFIER
Oligonucleotides		
Primers for plasmid construction	This paper	see Data S3
Primers for RT-qPCR	This paper	see Data S3
Primers for ChIP-qPCR	This paper	see Data S3
Recombinant DNA		
Plasmid: pCloneNAT1	Lab Stocks	N/A
Plasmid: pCloneHYG1	Lab Stocks	N/A
Plasmid: pCloneNAT1-hta1+H2A.X^{Sp}	This paper	N/A
Plasmid: pCloneHYG1-hta2+ H2A.X^{Sp}	This paper	N/A
Plasmid: pCloneNAT1-hta1+H2A.W^{At}	This paper	N/A
Plasmid: pCloneHYG1-hta2+H2A.W^{At}	This paper	N/A
Plasmid: pCloneNAT1-hta1+H2A.W.4A^{At}	This paper	N/A
Plasmid: pCloneHYG1-hta2+H2A.W.4A^{At}	This paper	N/A
Plasmid: pCloneNAT1-hta1+H2A.M.1^{Mpo}	This paper	N/A
Plasmid: pCloneHYG1-hta2+H2A.M.1^{Mpo}	This paper	N/A
Plasmid: pCloneNAT1-hta1+H2A.M.2^{Mpo}	This paper	N/A
Plasmid: pCloneHYG1-hta2+H2A.M.2^{Mpo}	This paper	N/A
Plasmid: pET15b-H2A.W	Osakabe et al.[19]	N/A
Plasmid: pET15b-H2B	Osakabe et al.[19]	N/A
Plasmid: pET15b-H3	Osakabe et al.[19]	N/A
Plasmid: pET15b-H4	Osakabe et al.[19]	N/A
Plasmid: pET15b-H2A.WΔCT	Osakabe et al.[19]	N/A
Plasmid: pET28a-H2A.Z	Osakabe et al.[19]	N/A
Plasmid: pET15b-H2A.W.4A	This paper	N/A
Plasmid: pGEM-T Easy-193 bp DNA	Osakabe et al.[19]	N/A
Software and Algorithms		
cutadapt v1.3-ictce-5.3.0-Python-2.7.6	[33]	https://cutadapt.readthedocs.io/en/stable/guide.html
bowtie2 v2.2.9	[34]	http://bowtie-bio.sourceforge.net/bowtie2/index.shtml
deepTools v2.2.4	[35]	https://deeptools.readthedocs.io/en/develop/
samtools v1.3	Li et al.[36]	http://www.htslib.org/
BEDTools v2.26.0	[37]	https://bedtools.readthedocs.io/en/latest/
IGV v2.4.1	[38]	https://software.broadinstitute.org/software/igv/download

(Continued on next page)

Continued

REAGENT or RESOURCE	SOURCE	IDENTIFIER
Star v2.5.3a	[39]	https://github.com/alexdobin/STAR
Htseq-count v0.6.1	[40]	https://htseq.readthedocs.io/en/release_0.11.1/count.html
R v3.5.1	R Foundation for Statistical Computing, Vienna, Austria	https://www.r-project.org/
ImageJ	[41]	https://imagej.nih.gov/ij/download.html
MACS2	Zhang et al.[42]	https://github.com/macs3-project/MACS
TrimGalore v0.6.2	Babraham Bioinformatics	https://github.com/FelixKrueger/TrimGalore
Picard v2.18	Broad Institute, Boston, MA	https://github.com/broadinstitute/picard
GraphPad Prism 8.0	GraphPad software	N/A
Other		
Ni-NTA agarose beads	QIAGEN	Cat#30250
HiLoad16/60 SP Sepharose HP	GE Healthcare	Cat#17113701
HiLoad16/600 Superdex200 pg	GE Healthcare	Cat#28989335
Model 491 Prep Cell	BioRad	Cat#1702927
Centrifugal concentrator Amicon Ultra 30K	Millipore	Cat#UFC903096

RESOURCE AVAILABILITY

Lead Contact
Further information and requests for resources and reagents should be directed to and will be fulfilled by the Lead Contact, Frédéric Berger (frederic.berger@gmi.oeaw.ac.at).

Materials Availability
Strains generated in the course of this work are freely available to academic researchers through the Lead Contact

Data and Code Availability
All raw read data and assembled sequence data that support the findings of this study have been submitted to the NCBI public sequence databases under accession number GSE152086. The study did not generate new code and used only open access softwares.

EXPERIMENTAL MODEL AND SUBJECT DETAILS

S. pombe strains and culture conditions
All the yeast strains used in this study are listed in Table S1. Yeast cells were grown at 32°C in YES (yeast extract with supplements) or EMM2 (Edinburgh minimal medium) with appropriate antibiotics for selection. For tetrad dissection, yeast cells were crossed on SPAS media for 2 days at room temperature and spores were dissected and analyzed to obtain the double mutant.[43]

METHOD DETAILS

MNase treatment assay
The reconstituted nucleosome preparation and MNase treatment assay was performed as described previously.[19,44] Briefly, nucleosomes (1.2 μg) were incubated with 0.024 U of MNase (NEB) in total of 60 μl reaction solution (30 mM Tris-HCl (pH 7.5), 5 mM NaCl, 2.5 mM $CaCl_2$ and 1.5 mM DTT) at 25°C for 1, 3, 6, 9 and 15 min. After incubation, 10 μl of each aliquot was mixed with deproteinization solution (20 mM Tris-HCl (pH 7.5), 80 mM EDTA, 80 mM EGTA, 0.25% SDS and 0.5 mg/ml proteinase K) to stop the reaction. DNA was extracted by phenol-chloroform and run non-denaturing 10% polyacrylamide gel electrophoresis in 0.5 × TBE (45 mM Tris,

45 mM boric acid and 1.6 mM EDTA). The native PAGE gel was stained with SYBR Green nucleic acid gel stain (Invitrogen) and DNA was visualized by ImageDoc (BioRad). The band intensity was analyzed by using ImageJ or Image Lab software (BioRad).

Phylogenetic analysis

Phylogenetic analyses of plant H2A was carried out following recommendation in.[45] Plant H2A sequences were identified through BLASTP[46] searches of published genomes[12–15,46–51] as indicated in Data S1 using *Arabidopsis thaliana* H2A sequences. Full-length sequences were aligned with MAFFT v7.427[52] using the default settings. Note, one sequence from *Selaginella moellendorffii*, 38507, was lacking a start codon, but inspection of the region upstream of the annotated gene yielded a start codon in-frame and the protein sequence was amended accordingly. The substitution model for maximum likelihood phylogenetic analysis was selected using ProtTest v3.4.2.[53] DAYHOFF+I+G was selected with an alpha value of 0.6923 and a p-invariant value of 0.0846. The maximum likelihood phylogeny was constructed with PhyML v3.3[54] with the following settings: -b −4 -d aa -m JTT -a 0.6923 -v 0.0846 –r_seed 1562932227 –no_memory_check. Branch supports were calculated using approximate likelihood ratio tests based on a Shimodaira-Hasegawa-like procedure.[55] Trees were visualized in FigTree v1.4.4. Plant H2A variants were identified according to criteria outlined in.[2,7] Both are recognized by long, K-rich C-terminal tails, with the KSPK motif specific to H2A.W. Full alignments, phylogenies and classifications can be found in Data S1.

Multiple sequence analysis

Select plant H2A C-terminal sequences were manually aligned in CLC Genomics Workbench 11.0 (https://digitalinsights.qiagen.com) based on regions proximal to the histone core domain and distal, with the distal region fixed on a proline residue including 4 amino acids upstream and all residues downstream. Sequences were aligned to show conservation of residues adjacent to this proline residue in the sequence logo, which was generated in CLC Genomics Workbench 11.0.

Construction of the yeast strains

Alleles containing C-terminal of histone H2A variants from different species were designed to integrate into C-terminal of H2A.α and H2A.β at their endogenous locus by homologous recombination using a plasmid-based method. Briefly, pCloneNat1 and pClone-Hyg1 were used to fuse the specific histone H2A C-terminal (*sp*H2ACT, *sp*H2A.W^{At}, *sp*H2A.W4A^{At}, *sp*H2A.M1^{Mpo} and *sp*H2A.M2^{Mpo}) to the endogenous C terminus of *sp*H2A.α and *sp*H2A.β in fission yeast by using natMX4 or hphMX4 cassette, respectively. For transformation, the plasmids were released from the vector backbone by restriction digestion and used to transform *Schizosaccharomyces pombe* by the lithium acetate method.[56] The genomic DNA from all constructed strains in this study were verified by PCR analysis and primers are listed in Data S3.

Yeast growth sensitivity assay

Cells were grown to mid-log phase in YES media at 32°C. Prior plating, cultures of all strains were adjusted to an OD_{600} equal to 1.0 and five-fold serial dilutions were prepared with sterilized H_2O. Of each dilution, 2 μL were spotted on YES plate containing various reagents and cells were grown at 32°C for 3-4 days. For heat sensitivity assay, cells were grown on YES plate at 37°C for 3 days. For cold sensitivity assay, cells were grown on YES plate at 16°C for 12 days. For Ura silencing assay, serial dilutions of indicated strains were grown at 32°C on EMM2 complete media and EMM media lacking Ura for 4 days. For growth curve assay, cells were growth to OD_{600} of 0.2 as starting point, keep growing at 32°C or 37°C or 2% v/v formamide (AppliChem, A3606) was added to liquid YES media and the cell density was measured in every four hours.

Histone extraction assay

Histones from indicated yeast strains were extracted by sulfuric acid and acetone precipitated method.[57] Approximately 1 × 10^8 exponentially growing cells were collected and resuspended in 500 μL NIB buffer (0.25 M sucrose, 60 mM KCl, 15 mM NaCl, 5 mM MgCl$_2$, 1 mM CaCl$_2$, 15 mM Pipes, pH 6.8, and 0.8% Triton X-100 containing protease inhibitors and PMSF). Cells were lysed by bead beating and lysate was then centrifuged at :19,000 g for 10 min at 4°C. Supernatant was discarded and pellet was resuspended in 0.4 M sulphuric acid for 1h. The supernatants were precipitated in 12 volumes of ice-cold acetone overnight. The precipitate was collected by centrifugation at 7000 rpm for 15 min at 4°C. The pellet was air-dried in a fume hood and resuspended in 100 μL of 4 M urea. Histones were subject to western blot analysis by using anti-H2A (Active Motif, 39235) and anti-H3 (Abcam, ab1791).

Live cell microscopy and imaging

Cells were grown in YES medium at 32°C until the exponential stage, 5 μL cells were stained with 5 μl of mounting solution with DAPI (VECTOR Laboratories, H-1200) at RT for 5 min. Microscopic analysis was performed using LSM700 point scanning confocal microscope with a Plan Apo 63x/1.40 Oil DIC M27 (Carl Zeiss) and images were displayed using Zeiss Zen lite software.

Transcriptome library preparation, sequencing and analysis

Cells were grown in YES overnight at 32°C to mid-log phase and harvested by centrifugation between OD_{600} of 0.6-0.8. When cultures reached OD_{600} of 0.3-0.4, cells were treated with formamide at a final concertation at 2% v/v for 4h. Pellets were washed once in water and then flash-frozen in liquid nitrogen and stored at −80°C. RNA was isolated using RNeasy Plus Mini kit (QIAGEN), then treated with DNA-free DNase Treatment & Removal (Invitrogen, AM1906).

Strand specific total RNA sequencing libraries were prepared from 500ng RNA using the NEB Ribo-Zero plus rRNA depletion Kit. Library quality control involved size determination by fragment analyzer (Advanced Analytical, High sensitivity NGS Fragment analysis Kit) and qPCR for quantification (KAPA library quantification Kit for Illumina). Samples were sequenced on the Illumina Hi-Seq2500 using single-end 50 bp sequencing at VBCF NGS Facility. Use bedtools v2.26 to transform bam-files to fastq for kallisto, then used Kallisto software (v0.43.1; kallisto quant–single -l 200 -s 20–plaintext -i transcripts.idx -o DIR sample) to calculate counts and tpms. Function Deseq2 in R (v3.3.1) was used to find differentially expressed genes between treated and untreated samples. Genes with False Discovery Rate (FDR) adjusted p value of 0.1 and log2 Foldchange of above 1 and below −1 were called differentially expressed. Statistical software R (v3.3.1) and the library DEseq2 was used to plot the results (log2fc_tr.untr versus -log10_padj_tr.untr). Fisher's exact test was performed in R (v3.3.1) for upregulated genes in subtelomeric heterochromatin. Downregulated genes and neutral genes were merged for the test (Data S2).

RT-qPCR analysis were performed as described previously.[58] cDNAs were quantified by qPCR using primaQUANT SYBR Master mix (Steinbrenner Laborsysteme GmbH) and a QuantStudioTM 3 Real-Time PCR system (Applied Biosystems/Thermo Fisher). Primers are listed in Data S3. For the calculation of mean values from independent experiments unless otherwise described.

Chromatin immunoprecipitation (ChIP)

Chromatin immunoprecipitation (ChIP) experiments were performed as described previously.[58] Briefly, 100 mL cell cultures were grown to OD_{600} of 0.4-0.6, crosslinked (1% formaldehyde, 20 min) and lysed by bead beating. The chromatin fraction was isolated and sheared to 200 bp-500 bp fragments using E220 Focused-ultrasonicator (Covaris). Immunoprecipitations (IPs) were performed overnight at 4°C with 4 μg of anti-H2A (39235, Active motif), 3 μg of anti-H3 (ab1791, Abcam), 4 μg of anti-H2A.Z (39640, Active motif), 4 μg of anti-H3K9me2 (ab1220, Abcam) and 4 μg of anti-Swi6 (ab188276, Abcam). Each IPs were coupled to 25 μL of ChIP-grade Protein A/G Magnetic Beads (#26162, Thermo Fisher scientific) at 4°C for 4 h. The beads were washed and eluted, and the eluate was reverse cross-linked overnight at 65°C and incubated with proteinase K and RNaseA for 2 h at 37°C. DNA was cleaned up with ChIP DNA Clean & Concentrator kit (Zymo Research). Immunoprecipitated DNA was quantified by qPCR using FastStart Essential DNA Green Master (Roche) and performed on the LightCycler® 96 Instrument (Roche). Primers are listed in Data S3. For the calculation of mean values from independent experiments unless otherwise described.

ChIP library preparation, sequencing, and analysis

Between 10-25 ng of immunoprecipitated DNA were processed for each ChIP-seq library preparation, following by NEBNext Ultra II DNA Library Prep Kit (Illumina) with the indexes provided in NEBNext Multiplex Oligos for Illumina (Index Primers Set 1, 2 and 3). The library size and concentration were determined by Fragment analyzer and Pico green analysis respectively, and libraries were pooled in equimolar amounts with up to 20 samples in each sequencing lane. Samples of at least 5 nM were multiplexed for sequencing on the Illumina Hi-Seq2500 using single-end 50 bp at VBCF NGS Facility. Transforming each samples in bam-format to fastq-format with bedtools (bam-tofastq -i *.bam -fq *.fq); Trimming the adaptors with cutadapt (cutadapt v1.3-ictce-5.3.0-Python-2.7.6; cutadapt -a A -o sample_tr.fq sample.fq); Mapping with bowtie2 (Bowtie2 v2.2.9; bowtie2 -X 1000 -p 10 -x GENOME sample_tr.fq -S sample.aligned_b2.sam); used samtools to transform sam-format to bam-format. Used annotation files: Schizo*Saccharomyces*_pombe_all_chromosomes.fa and spombe_all_chr_sorted.gff3 from https://www.pombase.org/. Calculation of the coverage normalized to the input with a log2 ratio (default parameters) and 10 bp length with deeptools (deepTools v2.2.4; bamCompare -b1 sample -b2 input -o sample_input_bs10b.l2rlnp.bw).

ATAC-seq

We conducted ATAC-seq as previously described using a home-made Tn5 that synthesized by Molecular Biology Service VBCF.[59,60] We performed experiment from two independent cultures ("replicates"). Briefly, 1×10^6 cells were grown to mid-log phase in YES media and washed twice in Sorbitol Buffer (1.4 M Sorbitol, 40 mM HEPES-KOH pH 7.5, 0.5 mM $MgCl_2$) + 10 mM BME. Then incubated in Sorbitol Buffer + 2 mM BME for 30 minutes, and spheroplasted in Sorbitol buffer with 0.25 mg/mL Zymolyase for 23 minutes, and then washed twice in Sorbitol Buffer. The spheroplasted cells were incubated in 10 μL of 1x TD buffer with 2 μL of Tn5 Transposase at 37°C for 30 minutes. For libraries preparation, we used NEBNext High-Fidelity 2x PCR Master Mix and Nextera index kit (Illumina) to amplify and barcoded transposed DNA fragments. In the PCR-variable experiment, we amplified the entire eluate until amplification curve reached its mid-log phase ($^1/_3$ of max signal), the number of PCR cycles required to reach this phase differed among samples and sequenced with paired-end 75 bp reads on Illumina Miseq. Bowtie2 was used to align *S. pombe* reads to ASM294v2.21 genome. The open chromatin regions were called using MACS2,[42] Peaks were filtered based on mappability of 35 bp sequences.

Adapters were first trimmed using TrimGalore version 0.6.2 (https://github.com/FelixKrueger/TrimGalore) and the resulting reads mapped to the *S. pombe* genome (ASM294v2.21) using Bowtie2 version 3.4.2.[61] Reads were filtered for a MAPQ score > 10 using SAMtools version 1.9 and subsequently filtered for duplicates using Picard tools MarkDuplicates version 2.18 (https://github.com/broadinstitute/picard).[36] Two independent biological replicates were merged for downstream analysis using SAMtools version 1.9. Bigwig coverage files to effective were generated using the deepTools version 3.1.2 utility bamCoverage using–effectiveGenomeSize 12631379–binSize = 10–smoothLength = 100.[62] Averaged ATAC-seq profiles were generated using the package EnrichedHeatmap with the normalizeToMatrix function and plotted using a custom script in R.[63]